Geochemistry International, Vol. 42, No. 12, 2004, pp. 1139–1153. Translated from Geokhimiya, No. 12, 2004, pp. 1285–1300.

Experimental Study of Gold Redistribution in a Shock-Metamorphosed Pyrite–Quartz Mixture with the Use of the ^{195}Au Radionuclide

S. M. Zhmodik*, N. V. Verkhovtseva*, V. F. Nesterenko, B. M. Chikov*, A. S. Zhmodik*, N. A. Nemirovskaya*, E. V. Airiyants*, and T. N. Moroz***

** United Institute of Geology, Geophysics, and Mineralogy, Siberian Division, Russian Academy of Sciences, pr. Akademika Koptyuga 3, Novosibirsk, 630090 Russia*

*** University of California, Gilman Drive, San Diego, La Jolla, CA 92092, USA*

Received July 30, 2003

Abstract—The behavior and distribution of gold in shock-metamorphosed rocks were studied experimentally. A gold-bearing pyrite–quartz (*Py–Qtz*) mixture was affected by shock waves by the method of impulse-shock loading of powdered materials ($P > 10$–15 GPa, $T > 2000$ K) with the use of the cylindrical shock load of a porous mixture to enable (due to Mach reflection of the shock waves) the unique neighboring development of a region of high dynamic pressure and temperature and a strongly deformed peripheral region of lower temperatures and densities with zones of localized shearing. This created favorable conditions for vapor formation in the central zone and the redistribution of this vapor in the surrounding material. The morphology of the strongly deformed peripheral region facilitated vapor diffusion. This process efficiently transported gold in the direction of Mach wave propagation and resulted in a significant increase in the gold concentration at the container bottom. A complex of methods, including β-autoradiography, was used to identify a heterogeneous, zonal vertical and horizontal distribution of gold in the compacted *Py–Qtz* mixture (compactite). The vertical section is marked by two maxima of gold concentration: at the level where melt appears and near the bottom of the container, where the amount of the silicate melt attains a maximum. In horizontal sections, above the level where melt appears the gold distribution is undulant. Below this level, the distribution is approximated by a parabolic function with a maximum at the center and minima near the container walls. During shock loading, much gold passed into the gas phase (perhaps in atomic and ionic modes or as compounds with sulfur) and precipitated in the form of "disseminated" gold (atomic, cluster, and nanoparticle modes of occurrence) on all minerals of the mixture (quartz and pyrite). The maximum gold concentrations in the compactite are restricted to the silicic melt. Gold evaporated throughout the process of impact loading with a Mach wave, which provides evidence that the kinetic energy was very heterogeneously transformed into internal energy at the shock wave front, mostly on the surfaces of particles. The mechanism of axial gold redistribution was related to gold evaporation at the front of the Mach shock wave and the radial propagation of vapor (or even jet-boiling) ahead of the front of the Mach shock wave.

INTRODUCTION

Mechanisms responsible for the redistribution and concentration of precious metals in rocks in the course of diverse energetic processes arouse the keen interest of researchers. A specific situation is the high-pressure transformations of rocks in such structures as astroblemes, earthquake foci, shear zones, deep-sitting structures under high lithostatic pressures, or structures produced by rheological explosions. The mechanisms and conditions of these transformations are understood inadequately, although studies in this field have been conducted and are still being continued [1–3]. The causes of high concentrations of precious metals in natural rocks affected by impact metamorphism (in astroblemes, meteorite craters) remain largely uncertain. We conducted impulse high-pressure loading of a gold-bearing pyrite–quartz (*Py–Qtz*) mixture with the aim of elucidating the behavior of gold and associated structural and compositional transformations under conditions when the material is affected by a shock wave of high amplitude and is adjacent to a region of a strongly deformed material, which was loaded by a shock wave with a low amplitude, including zones of localized shearing.

EXPERIMENT AND METHODS

Our experiment on shock loading was conducted using the approved method of impulse shock loading of mineral aggregates [4, 5]. The original (working) mineral mixture (that consisted of 0.1- to 0.25-mm size fractions) was a monomineralic powder of quartz from Brazil (with no more than 0.001% admixtures) and pyrite from the Ozerninskoe deposit, Buryatia, with the quartz to pyrite weight proportion equal to 1.75. The pyrite was preliminarily coated with gold by means of

its sorption from a diluted solution of gold chloride in distilled water with pH 5. The stable Au was doped with radioactive ^{195}Au (half-life 185 days; EC; γ). No gold was detected in the solution after sorption, and its concentration was 5×10^{-4} wt % in the pyrite and 2.85×10^{-4} wt % in the mixture. The mixture of pyrite and quartz with adsorbed gold was placed in a cylindrical steel container (working chamber L = 63 mm and d = 20.5 mm), which was then closed with a lower screw plug (Figs. 1a, 1b). The ring explosive charge utilized in the experiment was a 20-mm layer of ammonium nitrate (6ZhV) localized near the head of the container, with the shock loading conducted by the method of sliding detonation–directed ring loading of the container. The loading parameters were selected using the maximum charge permissible by the optimum preservation of the sample mass after passage of the shock wave (an increase in the charge thickness can result in the destruction of both the container and its filling).

After shock loading, the *Py–Qtz* powdered mixture was transformed into a rocklike compacted column (compactite), which was then additionally cemented with epoxy resin and sawed into equally spaced blocks (Fig. 2). The latter were polished with diamond polishing paste to prepare relief-free polished sections for further reflected-light, transmitted-light, and geochemical examination (regretfully, polished section III was lost during preparation). Simultaneously, part of the original pyrite–quartz mixture was cemented with epoxy resin to prepare a reference sample that was not affected by shock metamorphism, contained relatively equally distributed grains of quartz and pyrite (with adsorbed gold), and exhibited no traces of structurization typical of the compactite.

The quantitative and qualitative analysis of mineral phases in the *Py–Qtz* compactite was conducted on a Jeol scanning electron microscope equipped with a Kevex analytical setup (analyst S.V. Letov) and on a Camebax-micro microprobe (analyst O.S. Khmel'nikova). The spatial distribution of gold was registered and its relative concentrations were estimated quantitatively and qualitatively by β-autoradiography, using an AF film for autoradiography [6]. The numerical processing of the autoradiographs was conducted by a computer program complex for image analysis. The contents of

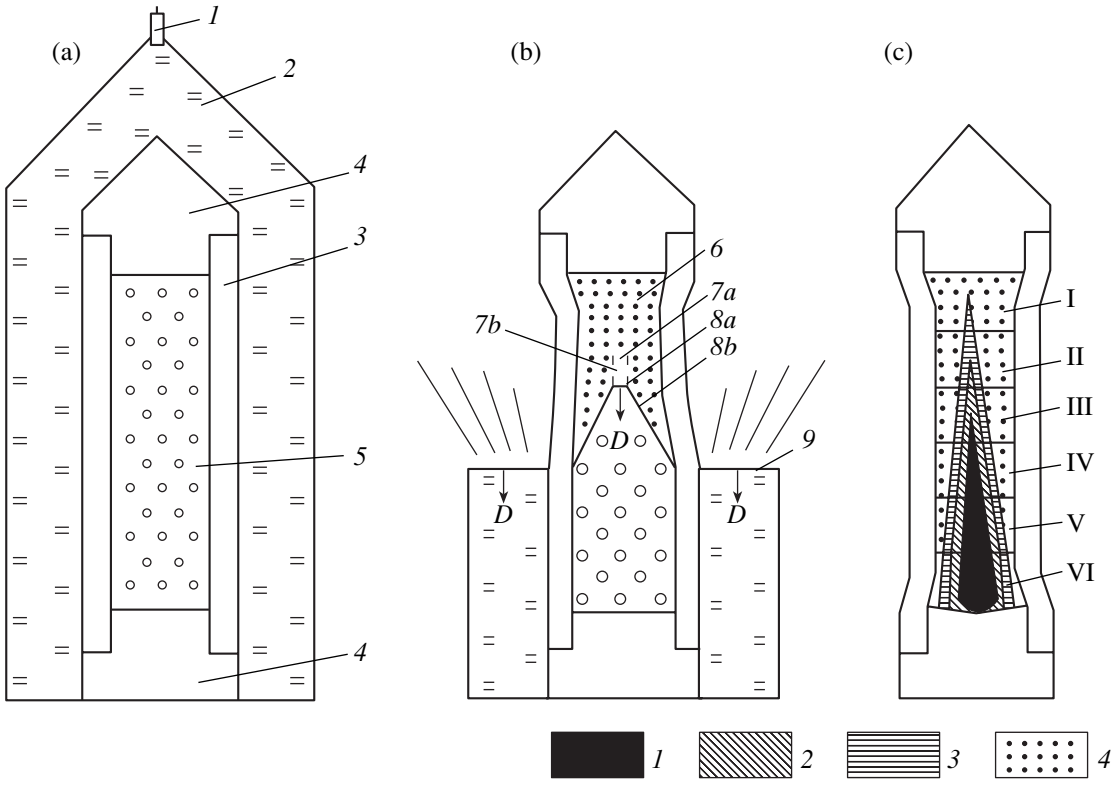

Fig. 1. Schematic representation of the experiment on the shock metamorphism of a gold-bearing *Py–Qtz* mixture. (a) (*1–5*) Equipment: (*1*) electric detonator; (*2*) explosive charge; (*3*) steel container wall; (*4*) metal plugs, (*5*) *Py–Qtz* mixture. (b) (*6–9*) Loading dynamics: (*6*) shock-metamorphosed compactite in (*8b*) the conical incident and reflected (not shown) shock waves; (*7a*) zone of high-velocity flow and high pressure (13.5 GPa) behind the front of the Mach shock wave; (*7b*) tangential break of the mass velocity; (*8*) shock wave front (*8a*—Mach shock wave, *8b*—conical wave); (*9*) detonation wave front. (c) Sections I–VI of the sample and its structural zoning (not to scale, see legend): (*1*) subzone of quartz melt and amorphization, $T > 2000$ K, $P \approx 13.5$–15 GPa; (*2*) subzone of sulfide melt, $T = 1973$–1448 K, $P < 13.5$ GPa; (*3*) subzone of porous Fe sulfide (pyrrhotite), $T = 973$–723 K, P from >1.9 to <13.5 GPa; (*4*) outer compactite zone, $T = 433$–723 K, $P \approx 1.9$ GPa. D is the velocity of detonation and the Mach shock wave.

sulfides in different zones of the compactite were counted on an ISA integration stage and by a computer. Phases newly formed during the experiment were identified by Raman spectroscopy, X-ray diffraction in a Gandolfi camera (analyst V.S. Pavlyuchenko), and microscopically (in reflected and transmitted light)

EXPLOSION PARAMETERS

Conditions at the Container Center behind the Mach Wave

The unusual conditions of shock loading in a cylindrical geometry are discussed in [7]. The central zone of the loaded sample in the cylinder is produced by the Mach reflection of a shock wave, and the parameters behind the Mach disk shown in Fig. 1b can be determined on the basis of this fact. For a stationary process, the velocity of the Mach shock wave is equal to the detonation velocity D. In our situation, the 20-mm layer of ammonium nitrate has a detonation velocity of 4.1 km/s [8]. Proceeding from the laws of conservation for a stationary shock wave [9], the following equations can be derived for a pressure P_M behind the Mach disk, specific internal energy E_M, and a temperature increase T_M:

$$P_M = \rho_0 D^2\left(1 - \frac{\rho_0}{\rho_s}\right),$$

$$E_M = \frac{D^2}{2}\left(1 - \frac{\rho_0}{\rho_s}\right)^2, \quad T_M = \frac{E_M}{C}.$$

The shock wave pressure and internal energy E_M were deduced from the laws of conservation for a stationary wave without any additional assumptions about the state of the material (except for the obvious assumption of a homogeneous distribution of the pressure, velocities of particles, and the density behind the shock wave). At the same time, the equation for temperature T_M is underlain not only by the assumption that the temperature distribution is homogeneous but also by additional assumptions that the potential energy is insignificant (these assumptions hold for our originally highly porous materials) and that there was neither melting nor any other phase transition. These assumptions mean that our estimate of T_M corresponds to the upper boundary for the homogeneous temperature behind the Mach wave. Nevertheless, this estimate is very useful for analysis of the mechanism responsible for the observed gold evaporation.

A review of metamorphism of quartz and the shock loading of simple quartz crystals at different original temperatures was presented in [10]. It was discovered that, under relatively low pressures of approximately 15 GPa, some quartz crystals are modified mainly by means of melting along gliding cracks when loaded with a flat shock wave. In our situation, the deformation conditions of quartz particles during the shock-induced compaction of the porous mixture are more complicated, and this could change the critical pressure of transformation compared to that of flat-wave loading.

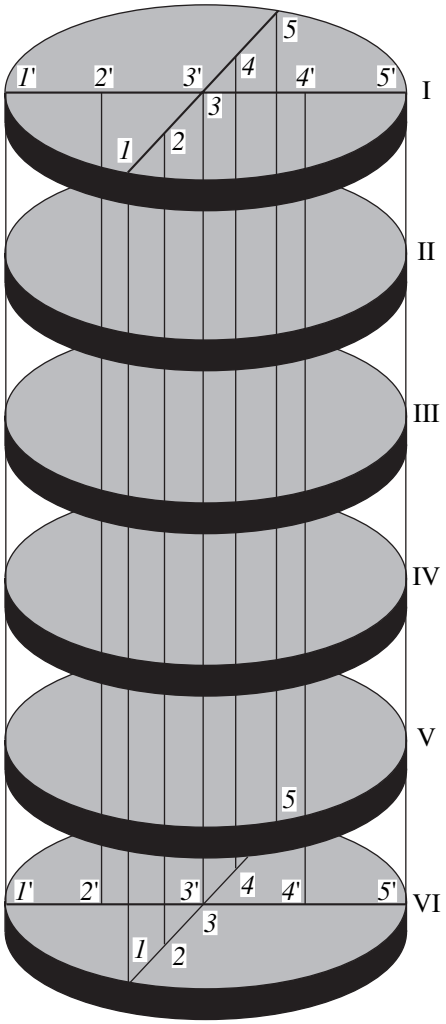

Fig. 2. Schematic representation of the compacted *Py–Qtz* mixture doped with ^{195}Au used to study the gold distribution by the autoradiography technique (Fig. 3). Numerals indicate points for which the distribution plots of the blackening intensity of ^{195}Au (Au concentration) were constructed in horizontal (*1'–5'*) and vertical (*1–5*) profiles in sections I–VI.

In these equations, ρ_0 is the original density of the porous mixture, which was equal to 1.72 g/cm^3, and ρ_s is the density of the material behind the Mach wave, which can be taken equal to the theoretical density of the mixture, which was 3.225 g/cm^3. Detonation velocity is 4.1 km/s. The heat capacity of the mixture (per mol) can be obtained from the rule $C = 3nR$ for each component, where n is the number of atoms in the molecule (for SiO_2 and FeS_2, $n = 3$). With regard for the relative masses of the components, $C = 1$ kJ/kg K. Including these values in the equation, we obtain P_M = 13.5 GPa, E_M = 1.83 MJ/kg, and a temperature increase T_M = 1830 K, which leads to a final estimate of the

homogeneous temperature of 2100 K at an initial temperature of 300 K.

These estimates imply the following conclusions. First and foremost, the homogeneous heating of the mixture behind a Mach wave cannot increase the temperature homogeneously to the gold evaporation temperature (3220 K) throughout the whole mixture volume. This means that the experimentally observed evaporation of gold resulted from the disequilibrated heating of the surfaces of particles during the shock-wave deformation of the porous mixture, as was discussed in detail in the review [11] of the nonequilibrium thermodynamics of shock-induced contraction. Evidently, this internal energy value can increase the temperature to a higher value than T_M obtained at the heterogeneous temperature distribution in the mixture, and this can bring about melting or even evaporating of this portion of the mixture. A simple estimation demonstrates that the value of energy E_M presented above is approximately five orders of magnitude greater than is necessary for the evaporation of all gold initially precipitated on the surface of pyrite particles. Second, this pressure estimate leads to the conclusion about the possibility of gas transitions under the effect of high pressure. The conditions necessary for the onset of evaporation in shock-loaded porous media were considered (without accounting for heterogeneous heating) in [12].

Conditions behind the Conical Wave in the Peripheral Part of the Container

The pressure and velocity of particles in the adjacent peripheral zone are much lower than behind the Mach wave [7] and can be estimated at $0.4\,P_D$ [13]

$$P_D = \frac{\rho_D D^2}{k+1},$$

where P_D is the detonation pressure, ρ_D is the density of the explosive (equal to 1 g/cm^3), k is a coefficient in the polytropic law for the dependence of the pressure on the density in the detonation products, $k = 2.5$ and $D =$ 4.1 km/s [8]. Based on this equation, we estimated the pressure behind the conical shock wave at 1.9 GPa, which is approximately seven times lower than the pressure behind the Mach wave. A similar value can also be obtained proceeding from the rotation angle of the outer part of the container (~5°). Under an analogous shock-pressure load [13] and under this detonation velocity D, the density behind the wave is approximately 1.404 times higher than the original one, as follows from the difference between the rotation angles for the inner and outer parts of the container [7]. The internal energy corresponding to these conditions of shock loading is 0.16 MJ/kg. The corresponding homogeneous temperature increase after a shock wave with this amplitude is 433 K (again, the potential energy remains unaccounted for, as was done above for the state behind the Mach wave). An additional temperature increase can take place owing to post-shock plastic flow, particularly at the loci of shearing, which is, however, hard to evaluate during this stage of our research.

It is pertinent to mention that, additionally to loading by the shock wave, the compressed material is also deformed due to the radial motions to the center, a process that is unstable because of localized shearing. The latter was studied in detail for aluminum oxide, silicon carbide, and a variety of reactant mixtures [11]. These localized deformations develop after shock loading and can result in the fragmentation of particles, additional heating, local melting, chemical reactions, and the sintering of the material under the effect of strong heating. The loci of localized shearing offer a useful model for certain types of geological faults in which analogous phenomena were observed. A single experiment provides the opportunity for studying numerous localized shear zones with different displacements, which are characterized by different displacement amplitudes at the boundary with the container. Thus, processes within these zones can be classed according to the extent of shear deformation. The method of a thick-walled cylinder provides a more developed structure of localized shear zones because of the presence of an original cavity at the capsule center [11].

STRUCTURAL TRANSFORMATIONS OF THE SHOCK-LOADED PYRITE–QUARTZ MIXTURE

The impulse loading of the container resulted in the predominantly adhesive compaction of the *Py–Qtz* mixture (with a more than 30% volume decrease) and its concentrically zoned structurization according to the general propagation scheme of the shock wave (Fig. 1c). Cross sections of the compactite column (Fig. 3a) exhibit a variety of discernible structural features: (1) intersecting arrays of localized shear zones along the planes of maximum shear stress; (2) an axial zone of amorphization, vitrification, and partial melting, corresponding to the Mach wave zone; (3) plastic flow and deformation zones (with subzones of sulfide melt and porous iron sulfide); and (4) the outer zone of the compactite arrived after the conical wave.

In addition to concentric zoning, the structure of the fractured compactite displays three systems of fractures, which are overprinted on one another. Among them, the most stable character is typical of two arrays of localized shearing. The configuration of these two arrays of localized shear zones is of a screw character with a divergence closer to the container walls, but the distribution of the fractures is characterized by the same direction as the systems of planar features and cracks in mineral grains, which are not constrained by the container walls. The stress-related genesis of localized shear zones in the compactite is beyond doubt and is typical of cylindrical contraction due to the loss of stability and the resultant localization of shearing along the planes of the maximum shear stress [11]. The third

system of shock-induced fractures is discernible only in the upper part of the container, particularly in section II. It developed in the form of a broken-line semicircle in the peripheral part of the section and, perhaps, resulted from the initial interaction of the shock wave, upper plug, and the walls of the container, which constrained the circular motion of the container wall and precluded the effective compaction of the neighboring layer. The sharpness of the zonal structure of the compactite increases downward, with the zones pronounced less clearly in the upper part of the container (sections I–II) than in its lower part (sections IV–V). The coordinates of the central zone relative to the container axis also changed.

The texture of the material corresponding to the "Mach" zone shows significant variations from section to section (Fig. 4), which are visible under a microscope. Photographs of section I display a round blob (d = 1.0–1.4 mm) of mostly fused grains of quartz, pyrite, and newly formed pyrrhotite. Conceivably, this aggregate resulted from the mechanical separation and accretion of mineral grains. In section II, the granular mass is transformed into a partly fused (vitrification, amorphization, and partial melting) aggregate (d = 0.18–0.3 mm) with anisotropic features (subvertical in the photograph) and an initial concentric zoning. The central part contains a visible oval (d = 0.2–0.3 mm) with melt in the interstitial space, which contains mostly pyrrhotite in the form of tiny droplets, hair-thin veinlets, and sometimes larger blobs. This level is marked by the appearance of pores and cavities.

The clear structurization of the axial zone can be seen in sections IV–V, in which concentric zoning is pronounced quite clearly (Fig. 5). The central zone of sections IV–V consists of the following subzones: (a) central channel (d = 0.2–0.25 mm); (b) a subzone of silicic melt with xeno- and idioblasts of newly formed moissanite (Fig. 6a); (c) a subzone with silicic melt and traces of deformations (mosaic extinction and planar features (Fig. 6b), radial fractures; d = 0.03–0.05 mm); and (d) a subzone (d = 0.05–0.1 mm) of the melt–crystalline aggregate transition with droplets of monosulfide solid solution of pyrrhotite composition.

Farther from the central channel, all sections display a zone of plastic flow and deformation (d = 2.5–2.8 mm), which is characterized by the absence of open fractures in both quartz and sulfides (Fig. 5). The sulfides most often preserve their original appearance but acquire a microporous, honeycomb cellular texture (Figs. 6d, 6e, 6f). Moreover, closer to its center this zone contains round grains, also with a texture cellular,

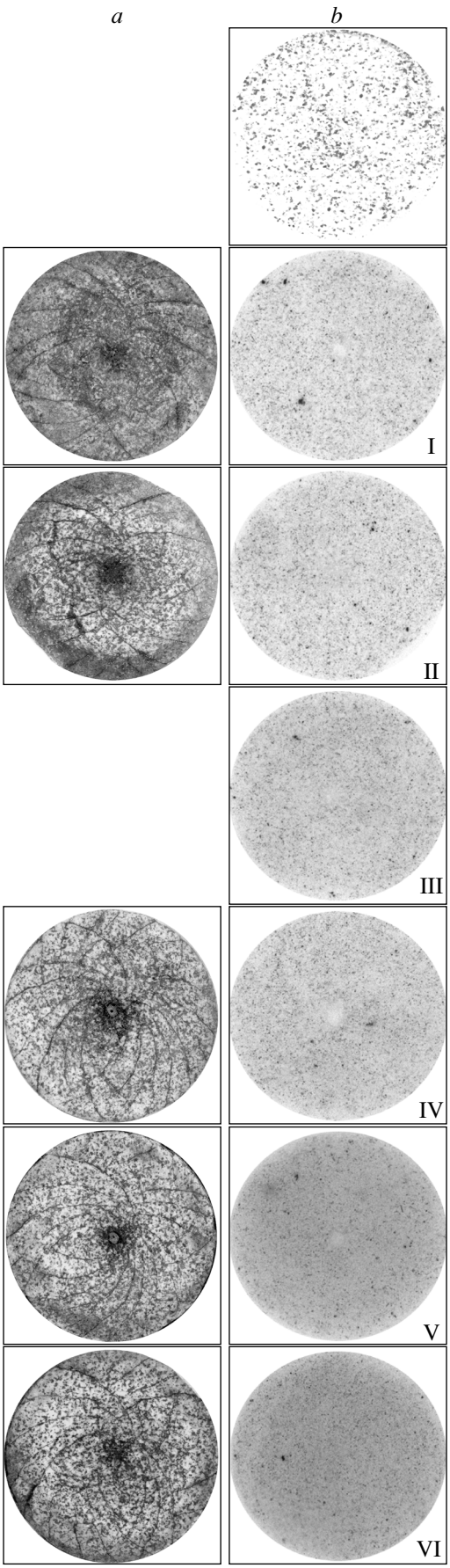

Fig. 3. Photographs of sections of the *Py–Qtz* mixture after shock-wave deformation (column *a*) and scanned autoradiograms (column *b*) exhibiting the distribution of gold in these sections. Thin arc lines in the sections of the compacted *Py–Qtz* mixture correspond to localized shear zones. The sections are 17.3 mm in diameter.

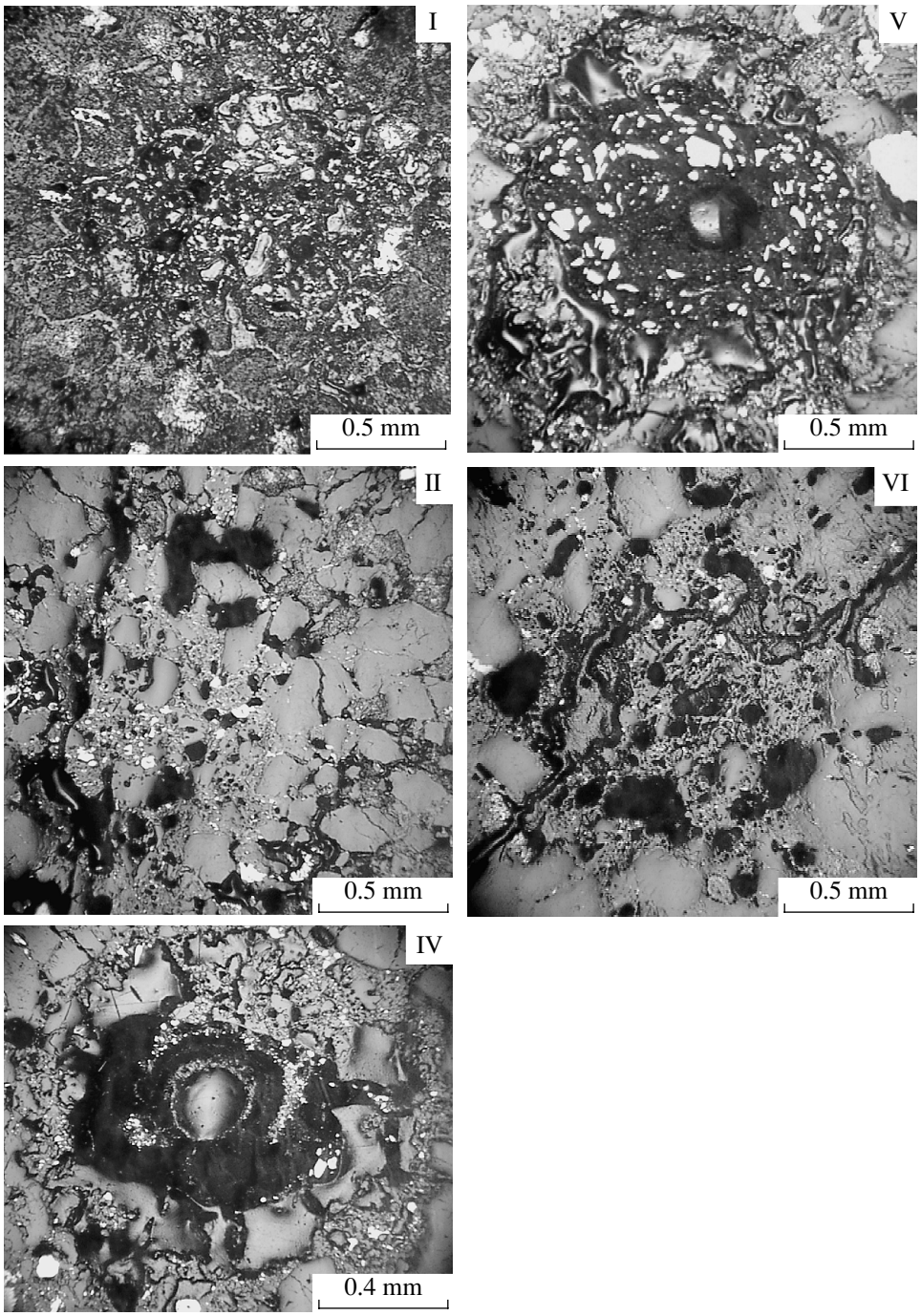

Fig. 4. Microphotographs of the central zone of the *Py–Qtz* mixture in the propagation direction of detonation. I–VI are sections of the column of the *Py–Qtz* mixture (from top to bottom, sample III was lost). The amount of melt obviously increases in this direction.

which are the source of sulfide material for the microfractures. Oriented subparallel microfractures in the quartz are healed with a silicic and silicic–sulfide melt.

The zonal structure and sizes of the axial zone in section V remain generally analogous to those in section IV (Fig. 5). The subzone of silicic melt is contrastingly separated and bears xeno- and idioblasts of silicon carbide. The transitional subzone is deformed and not as clearly pronounced. The maximum amounts of melt with rare drops of monosulfide solid solution (Fig. 6c) were identified in the axial zone in the lower part of the container (section VI), which is also characterized by anisotropy of its morphological features

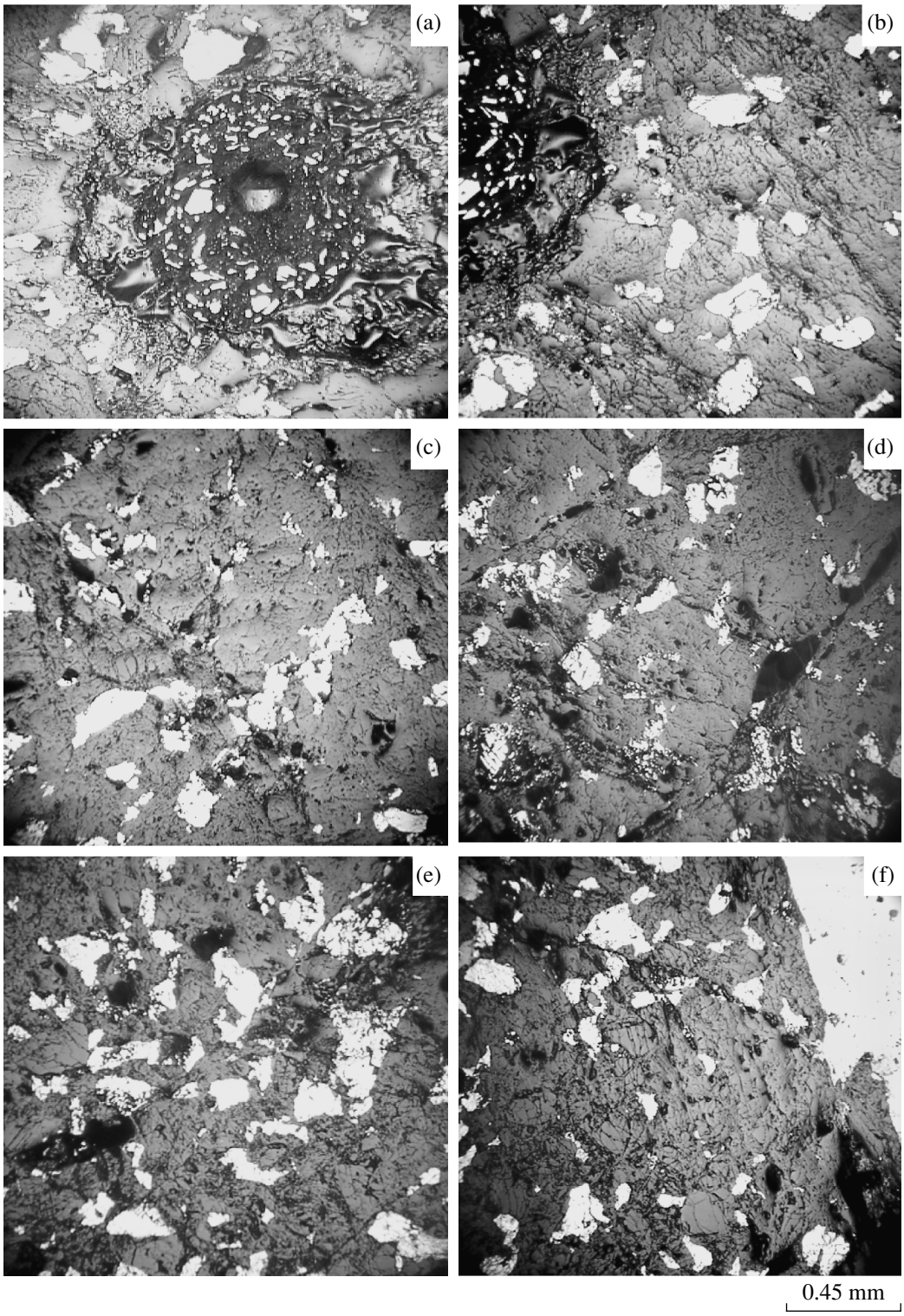

Fig. 5. Structure of the compacted *Py–Qtz* mixture in horizontal section V from (a) the central zone to the container walls; (e) profile bends on the mixture surface and container walls indicate a shear zone.

(diagonal in the photograph) with a random distribution of pores and voids and a poorly pronounced central oval structure (d = 0.2 mm) (Fig. 4).

The outer zone of the compactite has a much smaller volume than the axial zone and is not as clearly structurized, with the predominance of the mechanical redistribution of grains, becciation, and cataclasis. The zone consists of a granular aggregate of pyrite and quartz (Figs. 5c–5f). The results of quantitative mineralogical analysis indicate that the pyrite content is prone to

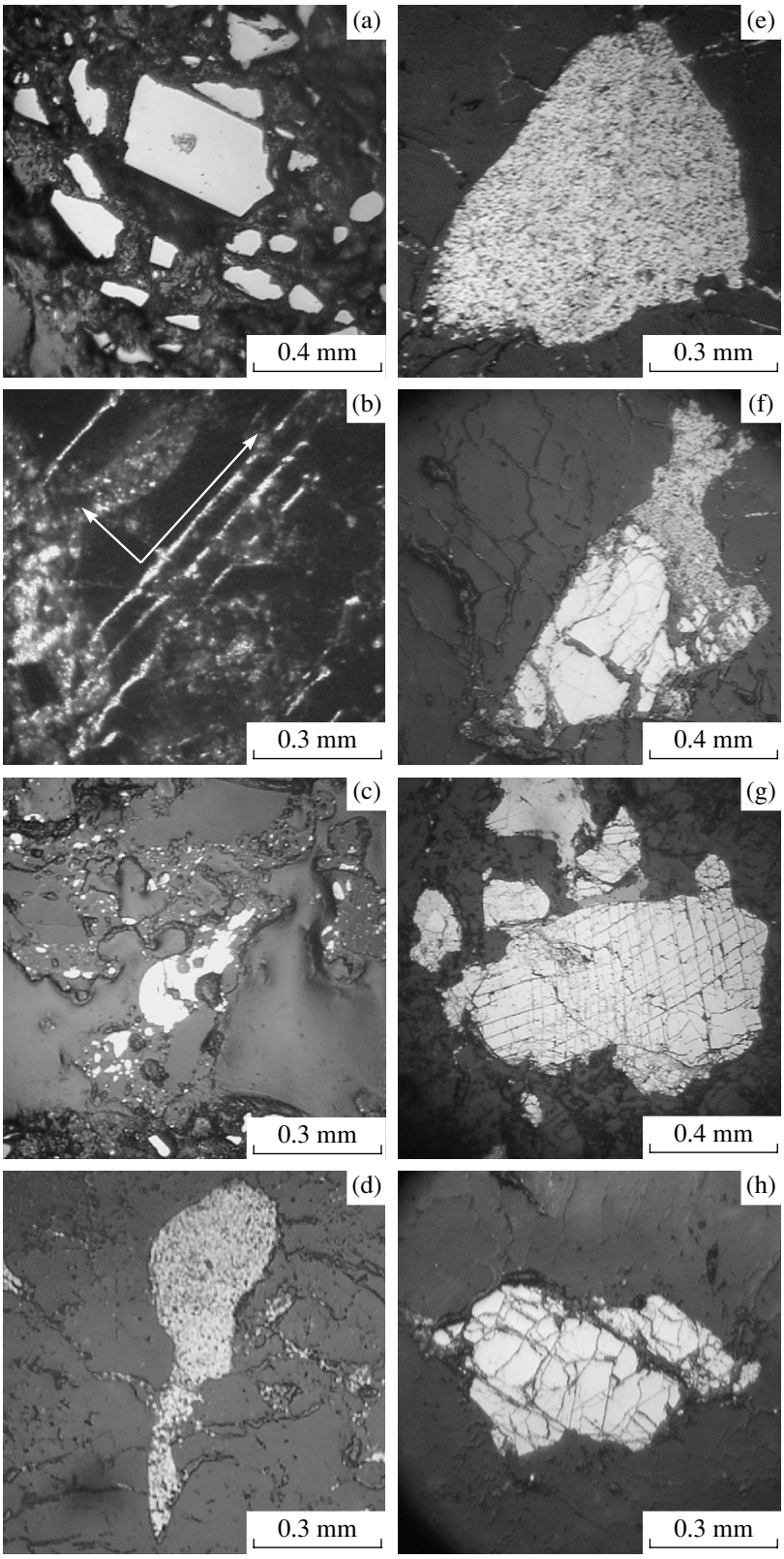

Fig. 6. Microphotograph of newly formed and altered minerals in the quartz–pyrite mixture after shock metamorphism. (a) Moissanite crystals and their fragments in melt. (b) Planar features in quartz; arrows indicate two arrays of the planar features. (c) Droplet of monosulfide solid solution and microfractures filled by sulfide as a result of flow. (d) Porous sulfide aggregates of pyrrhotite composition produced by the partial removal of sulfur. (e) Porous "honeycomb" pyrrhotite. (f) Pyrite grain partly replaced by pyrrhotite. (g) Two intersecting arrays of planar cracks in a pyrite grain. (h) Brecciated pyrite grains.

Table 1. Calculated contents (vol %) of minerals in horizontal sections I and V of the compacted *Py–Qtz* mixture

Sizes of the zone (circle radius and ring width, mm)	Quartz		Pyrite		Pyrrhotite		Melt		Moissanite	
	I	V	I	V	I	V	I	V	I	V
Central channel (0.15)	–	–	–	–	–	–	–	100	–	–
Subzone of *Qtz* melt (0.16)	–	–	–	–	–	–	–	65	–	35
Subzone of sulfide melt and porous sulfide	69.1	62.4	3.3	17.2	27.6	20.4	–	–	–	–
Outer compactite zone (2.0)	66.4	55.6	33.6	44.4	–	–	–	–	–	–
″ (2.0)	66.2	59.5	33.8	40.5	–	–	–	–	–	–
″ (3.0)	60.8	64.8	39.2	35.2	–	–	–	–	–	–

increase away from the center in the upper parts of the container (section I) and decrease in its lower part (section V) (Table 1). Mineral grains are sometimes displaced along localized shear zones (Fig. 5f), in which the plasticity of the *Py–Qtz* aggregate increases and it starts to fill fractures.

In general, the outer zone of the compactite is characterized by clearly pronounced zones of localized shearing, corresponding to a spiral stress field (Figs. 3, 5). At the same time, pyrite grains preserve their original morphology, and their distribution shows only very insignificant initial traces of ordering. Near the axial zone, the position of sulfide grains is often conformable with the contour of the zone (Fig. 5b). Away from the center, the long axes of the grains, pores, and voids become oriented orthogonally relative to fractures of one of the arrays in the form of bands that heal some localized shear zones of the same direction (Figs. 5c, 5d). Closer to container walls, the ordering in the distribution of pyrite grains and pores becomes less clear (Figs. 5e, 5f). As is seen under a microscope, quartz and pyrite grains are brecciated and cataclazed, and pyrite is sometimes cut by intersecting arrays of planar cracks (Figs. 6g, 6h).

MINERAL TRANSFORMATIONS IN THE SHOCK-METAMORPHOSED PYRITE–QUARTZ MIXTURE

In section V, which is characterized by the regime of Mach reflection of the shock waves, we examined in detail the composition of the newly formed and original phases of the *Py–Qtz* mixture. Analyses of the silicic and sulfide phases on a microprobe and scanning electron microscope are presented in Table 2 and Fig. 7.

The silicic melt near the central channel contains minor amounts of sulfur and iron. Quartz relics acquire a dark bluish color, but their composition remains absolutely the same as that of the original quartz. These quartz grains bear arrays of planar features intersecting at angles of ~90° (Fig. 6b). The subzone of silicic melt contains numerous anhedral grains and rare prismatic crystals up to 0.2 mm (Fig. 6a) with high reflectivity, comparable with that of iron. This phase is white and isotropic in reflected light. In oblique light, the crystals are transparent, with a weak yellowish green color. They contain 75–80% silicon, and this mineral was identified as moissanite, as was confirmed by X-ray diffraction data.

In the zone of the melt–crystalline aggregate transition, the composition of the droplets and equant sulfide blobs (Fig. 6c) corresponds to Fe-rich pyrrhotite with a high Fe/S ratio. The microporous sulfides from the zone of plastic flow and deformations become richer in sulfur (and the Fe/S ratio decreases) away from the axial zone. The highest sulfur concentrations were detected in the microporous pyrrhotite that partly replaces pyrite grains (Fig. 6f, Table 2). No changes were detected in the chemistry of quartz and pyrite in the outer zone of the granular compactite as compared with these minerals in the original sample. The material of the zone is ubiquitously variably cataclazed, fragmented, and brecciated, and the *Py–Qtz* aggregates in the localized shear zones are mylonitized.

GOLD DISTRIBUTION IN THE SHOCK-METAMORPHOSED PYRITE–QUARTZ MIXTURE

The thorough blending of the starting materials provided a fairly homogeneous gold distribution in the working *Py–Qtz* mixture. The heterogeneities identified in the gold distribution of the compactite were caused by the behavior of the metal and its redistribution during the impulse shock loading.

The following results were obtained by numerical processing of β-autoradiographs, which document the distribution of ^{195}Au after the experiment in six sections of the Au-bearing *Py–Qtz* mixture (Figs. 3b, 8). Two modes of gold occurrence in the *Py–Qtz* mixture were identified: adsorbed on the surface of pyrite grains and disseminated throughout the volume of the mixture. Rare tiny patches with elevated gold concentrations (spots with the maximum blackening of the nuclear

Table 2. Microprobe analyses (wt %) of minerals in horizontal section V of the compacted pyrite--quartz mixture

Zone, subzone	Mineral	Fe	Cu	Si	Al	S	K	Ca	Total
Quartz melt and amorphization	Moissanite	0.10	0.00	79.88	0.00	0.00	0.01	0.00	79.98
	Moissanite	0.17	0.00	80.03	0.02	0.01	0.02	0.00	80.25
	Moissanite	0.13	0.00	80.05	0.00	0.00	0.00	0.00	80.19
	Moissanite	0.25	0.00	79.63	0.00	0.00	0.03	0.01	79.93
	Quartz	0.21	0.00	46.77	0.00	0.02	0.03	0.01	47.04
Sulfide melt	*MSS* droplet	57.79	0.00	0.02	0.00	39.88	0.002	0.01	97.70
	MSS droplet	60.10	0.00	0.10	0.00	39.07	0.04	0.00	99.94
	Quartz	0.06	0.00	45.99	0.00	0.01	0.03	0.01	46.09
	Quartz	0.01	0.00	45.55	0.00	0.19	0.03	0.03	45.95
Porous Fe sulfide	Porous *Pyrr*	62.35	0.00	0.16	0.00	37.50	0.03	0.01	100.05
	Porous *Pyrr*	58.76	0.00	0.00	0.00	40.04	0.00	0.00	98.80
	Rims of porous *Pyrr**	61.00	0.00	0.29	0.00	39.10	0.03	0.06	100.48
	Fargmented pyrite*	46.78	0.02	0.00	0.00	53.17	0.00	0.00	99.98
	Quartz	0.08	0.00	46.28	0.00	0.01	0.01	0.01	46.39
	Quartz	0.06	0.00	46.97	0.00	0.00	0.04	0.00	47.07
Outer zone of the compactite	Fargmented pyrite	45.60	0.01	0.00	0.00	52.88	0.01	0.01	98.51
	Fargmented pyrite	45.74	0.00	0.03	0.00	53.50	0.06	0.00	99.33
	Pyrite	46.54	0.00	0.08	0.00	53.07	0.01	0.00	99.70
	Pyrite	46.83	0.00	0.00	0.00	53.35	0.00	0.00	100.18
	Quartz	0.07	0.00	46.56	0.00	0.01	0.00	0.00	46.64
	Quartz	0.11	0.00	45.27	0.00	0.21	0.01	0.14	45.75

Note: Analyses were conducted at the Analytical Center of the United Institute of Geology, Geophysics, and Mineralogy, Siberian Division, Russian Academy of Sciences, Novosibirsk, on a Camebax-Micro microprobe, analyst O.S. Khmel'nikova. *Pyrr* = pyrrhotite.

* Analyses of a single iron sulfide grain.

emulsion) correspond to single chalcopyrite grains accidentally occurring in the starting pyrite concentrate. The sorption capacity of chalcopyrite with respect to gold is known to be much higher than that of pyrite [14, 15].

First of all, the gold concentration in the compactite is prone to increase downward, as follows from the systematic variations in the optical density of the blackening of the nuclear emulsion in the autoradiographs (Figs. 3b, 9). Gold precipitation in the outer zone of the compactite is virtually independent of the state of the mineral aggregate but is directly correlated with the sizes of the zones where high energy was released after the passage of the Mach wave (localized shearing zones) and the amount of melt in the axial zone (Figs. 8, 10). The gold concentration in the lower part of the container unmonotonically increases by a factor of nearly three compared to its upper part. The first relative increase was detected in section III (Figs. 9, 10), in which the first melting was identified, and the second gold maximum falls onto the lowermost part of the container (section VI), which is marked with the most extensive melting).

DISCUSSION

The compression of the *Py–Qtz* mixture under the effect of a shock wave resulted in the following concentric zoning (from the container center to its walls): an axial zone with a central channel, which is filled with melt in the lower and upper parts of the container and remains empty in its middle part; a zone of silicic melt with moissanite xeno- and idioblasts, quartz relics with planar features, and droplets of monosulfide solid solu-

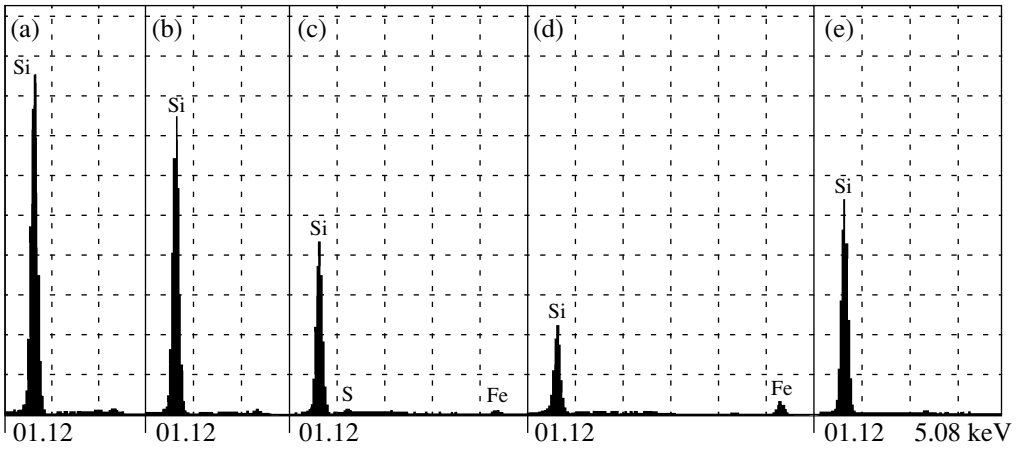

Fig. 7. Energy dispersive spectra of the Si-bearing phases in the compacted *Py–Qtz* mixture. (a) Standard (99.99 wt % SiO_2). (b) Moissanite from the melt zone. (c) Sulfur- and iron-bearing silicic melt. (d) Iron-bearing silicic melt. (e) Quartz.

tion near the margin of the zone; a zone of plastic flow and deformations with microporous pyrrhotite; and a zone of predominantly brittle deformations (granular compactite) with ubiquitous brecciation and cataclasis.

The concentric zoning is cut by variably directed spiral shear planes, which produce interference patterns in cross sections and look like spiral lines. These zones are marked by the significant mechanical displacement of minerals, plastic flow (particularly of pyrite), and fragmentation of the material practically throughout the whole lengths of the zones. This creates undulant distribution patterns of minerals and gold (Figs. 8, 10). The intersection of these zones is marked by planar features in pyrite. A comparison of the major stress trajectories in our experiment with the results of tectonic modeling demonstrates that our data are compatible with rotational models in the systematics of shear zones. Structures of this type (arc, semicircular, and concentric strike-slip faults) suggest the rotation of blocks in the spiral field of normal stress and the concentric field of radial stress (Fig. 11) [16].

According to the systematics of shock metamorphism stages in [17, pp. 15, 19], planar features develop in quartz at temperatures and pressures of 373–573 K and >5–15 GPa, respectively. Arnold's [18] method indicates that the temperature within the zone of plastic flow from pyrrhotite droplets to pyrite that is partly transformed into microporous pyrrhotite should be 973–723 K. This estimate is in agreement with data on the pyrite dissociation temperature (963 K). Within the localized shear zones, the temperature outside regions with plastic deformations seems to have been below 723 K, as follows from the absence of pyrrhotite in them. Analogous temperature values (723–733 K) occurred in the zone of brittle deformations. The temperature in the zone with droplets of monosulfide solid solution could correspond to the melting temperature of pyrrhotite (1448 K). The calculated temperature and pressure values are also in agreement with these data and correspond to 2130 K at 13.5 GPa for the central zone (behind the Mach wave) and 433 K at 1.9 GPa for the peripheral zone of the granular compactite (behind the conical wave). The absence of sulfides from the melt zone and pyrite transformation into pyrrhotite in the zone of plastic deformations testify that some sulfur passed into the gas phase. The amount of sulfur transformed into gas was 336 g/mol S. Iron evaporated exclusively from the melt zone. Iron and sulfur most probably occurred in the gas phase in the ionic or atomic modes because of the high velocity of the shock contraction and the brief duration of the high-pressure stage (approximately 10 μs).

Gold occurred in pyrite before the experiment in the adsorbed mode. It is known that, regardless of the genesis of pyrite (high- or low-temperature hydrothermal or supergene), Au in this mineral without admixtures of As, Sb, or other conductor elements occurs on the surface of crystals [6]. These data and the detailed results of experiments suggest that the sorption mode is the main mode of gold occurrence in pyrites [19, 20]. The data of precise studies with the use of the ESXA technique have demonstrated that gold adsorbed on the surface of pyrite composes an individual phase or clusters [21, 22]. Thus, gold adsorbed on pyrite which was used in our experiment is a typical mode of gold occurrence in natural pyrite that does not contain significant concentrations of conductor elements, primarily arsenic.

The analysis of the β-autoradiographs that demonstrate the distribution of gold in the *Py–Qtz* mixture after shock metamorphism reveals the following feature of its distribution. There are at least two modes of gold occurrence; adsorbed on the surface of pyrite grains and disseminated throughout the *Py–Qtz* mixture, with the latter detected in all zones, including the zones of silicic melt, plastic deformations, and the outer compactite zone.

No significant amount of gold precipitated on the walls of the iron container, or, at least, no local maxima

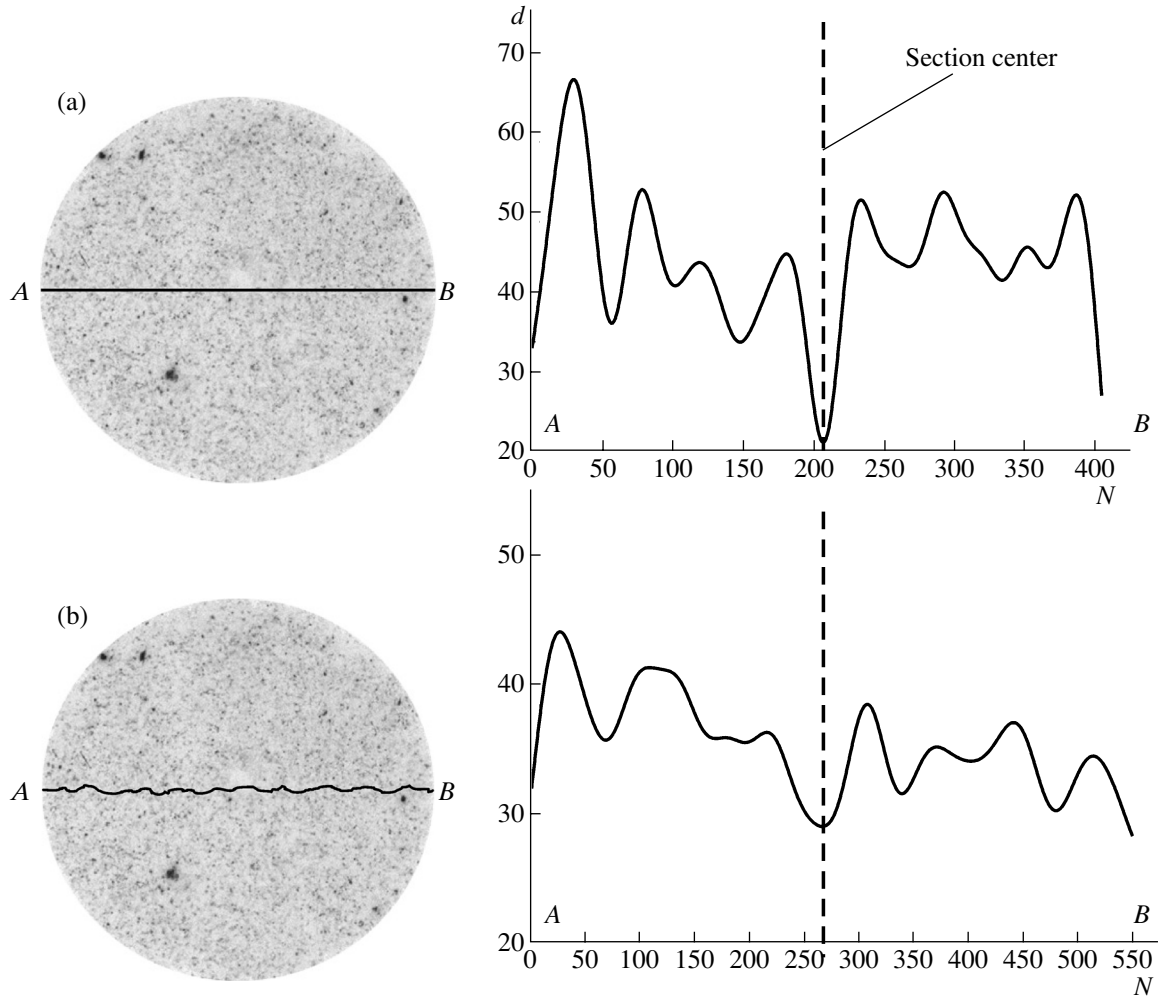

Fig. 8. Autoradiographs and smoothed (degree of smoothing = 20) gold distribution patterns along profile *A–B*, section I: (a) is the profile of gold distribution irrespective of its mode of occurrence in the shock-metamorphosed *Py–Qtz* mixture; (b) is the profile of gold distribution for the disseminated mode of its occurrence in the shock-metamorphosed mixture. The gold distributions are similar in both situations. Horizontal axis: number of spots (*AB* distance is 17.3 mm); vertical axis: blackening density (*d*) of the nuclear emulsion, which is proportional to the gold concentration.

were identified on the inner surface of the container. Conceivably, small gold concentrations could be "implanted" into the iron container to a depth of ≈0.2 mm from the surface of its walls, but the gold concentration was lower in this layer than in the *Py–Qtz* mixture adjacent to the walls of the container.

In the vertical section of the compacted *Py–Qtz* mixture, the gold concentration increases downward on average by a factor of three. The gold distribution throughout the whole profile is undulatory, with a first increase in its concentration (section III) before the region with the first appearance of melt. Another maximum corresponds to the lower part of the container with the highest amount of melt. Thus, gold was transported during the shock loading along the direction in which detonation propagated and was deposited in the most significant amount at the level with the maximum temperature and pressure. There are good reasons to believe that significant gold amounts could be lost from the lower part of the container if its tightness was disturbed. Gold precipitation outside the melt zone (crater) is virtually independent of the composition of the minerals. At the same time, high gold concentrations were unambiguously detected in the silicic melt in the lower part of the container, where gold concentrations are two to three times higher than in the melt in the upper part of the container. The mechanism of this gold redistribution could be related to its evaporation at the front of the Mach shock wave, before the material completely consolidated. A certain amount of the vapor expanded, "snowballed" before the front of the Mach shock wave, and could effectively transport gold toward the container bottom, thus increasing the gold concentration there.

The distribution of gold in horizontal profiles of the compacted *Py–Qtz* mixture is also uneven (Fig. 10).

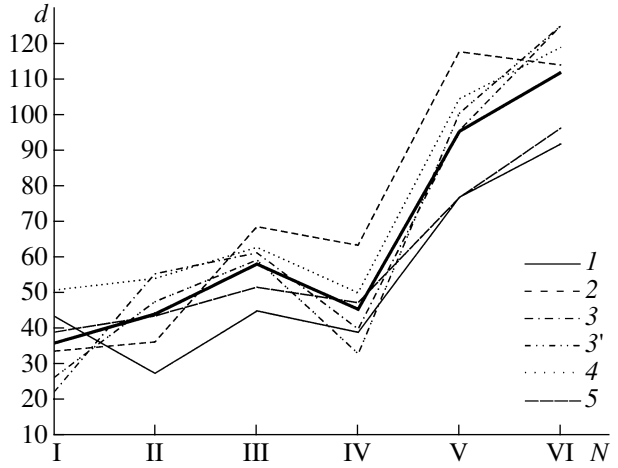

Fig. 9. Gold distribution in the vertical section of the compacted gold-bearing *Py–Qtz* mixture (results of numerical processing of autoradiographs). Horizontal axis: sections I–VI (see Fig. 2); vertical axis: blackening density of the nuclear emulsion (proportional to the gold concentration). The heavy line presents averaged values. No gold distribution is shown for lines *1*', *2*', *4*', and *5*' (Fig. 2), because they coincide with the lines shown in the diagram. The accuracy of the measurements can be evaluated using lines *3* and *3*'.

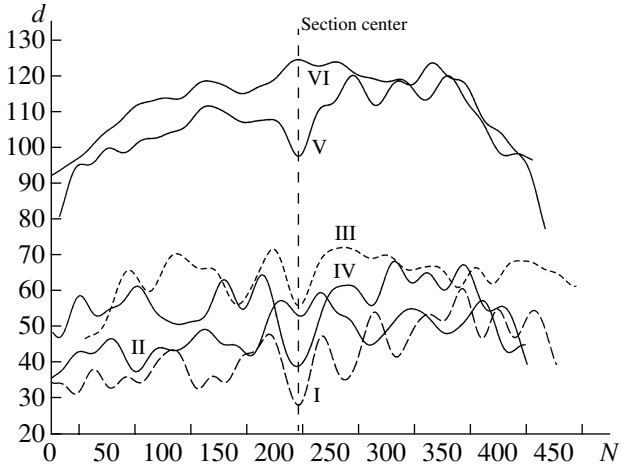

Fig. 10. Gold distribution along horizontal profiles in sections (I–VI) (Fig. 2) of the compacted *Py–Qtz* mixture (results of numerical processing of autoradiographs). Horizontal axis: number of spots (profile length is 17.3 mm); vertical axis: blackening density of the nuclear emulsion.

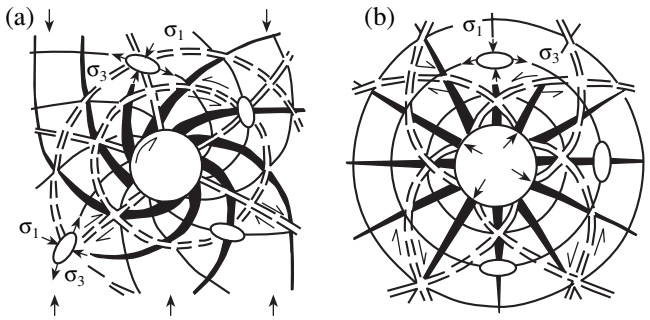

Fig. 11. Results of tectono-physical modeling of the structure of arc, spiral, circular, and concentric shear zones in (a) a spiral and (b) a concentrically radial (stationary model) fields of shear stress (after Bondarenko [16]); σ_1 and σ_3 are the major stress trajectories.

The character of gold distribution is obviously undulatory, particularly before sections in which melt appears in the central channel. The maximum gold concentrations are definitely restricted to the arc zones of localized shearing. In other words, gold is removed from the upper parts of the compactite, where the central channel is destructed most strongly, and enriches the nearby material, with maxima at local shear zones, which seem to have served as conduits for the preferable transport of the vapor. The central zone in the lower part of the container is the richest in gold. This character of the patterns in the horizontal section of the compactite suggests that pressure played a significant role in gold deposition. It is difficult to more accurately evaluate the horizontal pressure variations in the container. The volumetric concentration of pyrite suggests that the contents of iron sulfides are prone to increase toward the walls of the continents from 30.9 to 39.2 vol % in the upper part of the container at a simultaneous decrease from 45 to 35 vol % in its lower part, with an undulatory distribution of minerals in the profiles. The gold concentration decreases in the same direction (Fig. 12), a fact indicating that gold is predominantly contained in the disseminated mode, which is only weakly correlated with sulfides.

The parameters of our experiment imitate those of fast processes. Calculations indicate that the shock load lasted for approximately 10 μs at a detonation velocity of ammonium nitrate (6ZhV) of 4.1 km/s, with the heating and cooling rates of the loaded minerals also being fast [23, 24]. Such parameters can be achieved in nature mainly during the impact of cosmic bodies and the development of astroblemes (from 3.8×10^{16} to $4.2 \times$

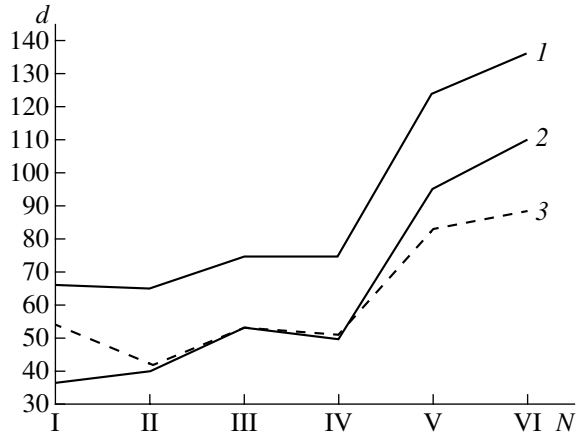

Fig. 12. Variations in the average gold concentration (blackening density of the nuclear emulsion *d*): (*1*) gold adsorbed on pyrite, (*2*) disseminated gold, and (*3*) estimate for the whole area of the section for sections of the compacted *Py–Qtz* mixture; *d* = 75 corresponds to a gold concentration of approximately 2.8 ppm.

10^{23} J), meteoritic craters, nuclear explosions (from 10^{12} to 2.4×10^{17} J), endogenic "impactogenesis" in zones and traps with hydrocarbons (from 6.3×10^{10} to 3.6×10^{17} J), and at earthquake foci (from 10^{15} to 10^{18} J), with the shock wave of an event with a magnitude of 8 on the Richter scale attaining a velocity of approximately 2 km/s [25–27]. The utilization of these data in application to other processes demands proof that these processes were fast. At the same time, our results can be used in explaining the mechanisms responsible for the development of global geochemical anomalies that could be related to the impact of cosmic bodies [28] and the potential possibility of gold redistribution and concentration within certain areas near impact structures, particularly in the presence of water. Perhaps ultrahigh pressures can also be achieved during local stress relief within collision zones [29, 30].

CONCLUSIONS

Our experiment on the shock-wave deformation of a *Py–Qtz* mixture at $P > 10$ GPa and $T > 2000$ K (in the central zone) led us to draw the following conclusions:

(1) Much of the gold contained in the material passes into the gas phase (perhaps in the atomic form or as compounds with sulfur) during the shock load and then precipitates in a disseminated mode (atomic gold, clusters, and nanoparticles). Gold precipitates on all minerals of the mixture (quartz and pyrite) but does not enrich the iron walls of the container.

(2) The compacted *Py–Qtz* mixture is characterized by certain horizontal and vertical distribution patterns of gold. The vertical section has two maxima of gold concentrations: at the level where melt appears and near the bottom of the container, where silicic melt is formed (the main maximum). The horizontal distribution of gold is undulatory to the level where melt appears (section VI). The gold distribution at the melt level is described by a parabolic function (from the container center to its walls) with a maximum at the center and minima near the walls of the container. The undulatory pattern of gold redistribution could be caused by its preferable diffusion along localized deformation zones and precipitation on the greater surface area of the fragmented particles. The significant increase in the gold concentration in the vertical direction could be caused by the expansion of the gold-bearing vapor (or even jet injections) before the Mach wave and by the snowball effect.

(3) The maximum gold concentrations in the compactite occur in the silicic melt.

It is pertinent to mention that the mechanisms and factors of gold deposition are unusual. It is well known that gold acts in most processes as a siderophile and chalcophile element [6]. These characteristics of gold were not, however, exhibited in our experiment, probably because gold was transported in a principally different mode, namely, in the atomic state and as nanoparticles. Our data can be used in analyzing geochemical anomalies in rocks resulting from fast processes related to impact events [28, 31–35].

ACKNOWLEDGMENTS

The authors thank A.I. Solov'ev and S.V. Zinov'ev for significant help during the initial stage of this research and S.A. Vishnevskii for valuable consultations.

This study was supported by the Russian Foundation for Basic Research, grant no. 03-05-64563, and the Presidium of the Siberian Division, Russian Academy of Sciences, grant nos. 6.4.1 and 161.

REFERENCES

1. A. A. Deribas, N. L. Dobretsov, V. M. Kudinov, and N. I. Zyuzin, "Impact Compression of SiO_2 Powders," Dokl. Akad. Nauk SSSR **168** (3), 665–668 (1966).
2. A. A. Marakushev, "Thermodynamics of the Systems of Geochemical Mineral Facies," Geokhimiya, No. 12, 1251–1265 (2000) [Geochem. Int. **38** (12), 1147–1160 (2000)].
3. O. I. Yakovlev, "Differentiation Mechanisms of Planetary Matter under the Effect of High-Velocity Impacts," in *Cosmochemistry and Comparative Planetology* (Nauka, Moscow, 1989), pp. 127–142 [in Russian].
4. V. F. Nesterenko, *Impulse Loading on Heterogeneous Materials* (Nauka, Novosibirsk, 1992) [in Russian].
5. B. M. Chikov, "Shear Stress Structuring in the Lithosphere: Varieties, Mechanisms, and Conditions," Geol. Geofiz., No. 9, 3–39 (1992).
6. A. G. Mironov, A. I. Al'mukhamedov, and V. F. Geletii, *Experimental Study of Gold Geochemistry by the Method of Radioisotopic Indicators* (Nauka, Novosibirsk, 1989) [in Russian].
7. N. A. Kostyukov and G. E. Kuz'min, "Development Criteria of the Central Zone-Type Macroheterogeneities in Shock-Wave Loaded Porous Rocks," Fiz. Goreniya Vzryva, No. 5, 87–96 (1986).
8. M. Adamets, V. S. Zlobin, and V. V. Kiselev, "Experimental Determination of the Rotation Angle during the Explosion-Caused Acceleration of a Plate," in *Treatment of Material by Loading Impulses* (Nauka, Novosibirsk, 1990), pp. 211–215 [in Russian].
9. Ya. B. Zel'dovich and Yu. P. Raizer, *Physics of Shock Waves and High-Temperature Thermodynamic Phenomena* (Fizmatgiz, Moscow, 1963) [in Russian].
10. A. J. Gratz, W. J. Nellis, J. M. Christie, *et al.*, "Shock Metamorphism of Quartz with Initial Temperatures –170 to 1000°C," Phys. Chem. Minerals **19**, 267–288 (1992).
11. V. F. Nesterenko, *Dynamics of Heterogeneous Materials* (Springer, New York, 2001).
12. A. H. Shen, T. J. Ahrens, and J. D. O' Keefe, "Shock Wave Induced Vaporization of Porous Solids," J. Appl. Physics **93** (9), 5167–5174 (2003).
13. A. A. Shtertser, "Determination of Pressure Characteristics in Porous Bodies Compressed by a Strong Explosive Mixture through a Metallic Plate," Fiz. Goreniya Vzryva, No. 1, 141–143 (1982).

14. A. G. Mironov and S. M. Zhmodik, "Gold Precipitation on Sulfides: Evidence from Autoradiography of ^{195}Au," Geokhimiya, No. 7, 985–991 (1980).
15. S. M. Zhmodik and E. V. Airiyants, "Experimental Study of Low-Temperature Interaction of Sulfides and Precious Metal Solutions of Au, Ag, and Ir," in *Water–Rock Interaction* (Balkema, Rotterdam, 1995), pp. 841–844.
16. P. M. Bondarenko, "Modeling of Tectonic Stress Fields in Elementary Deformation Structures," in *Experimental Tectonics: Methods, Results, and Horizons* (Nauka, Moscow, 1989), pp. 126–162 [in Russian].
17. *Impactites*, Ed. by A. A. Marakushev (Mosk. Gos. Univ., Moscow, 1981) [in Russian].
18. R. G. Arnold, "Equilibrium Relations between Pyrrhotite and Pyrite from 325 to 743°C," Econ. Geol. **57** (1), 521–529 (1962).
19. V. L. Tauson, T. M. Pastushkova, and O. I. Bessarabova, "Concentration Limits and Modes of Occurrence of Gold in Hydrothermal Pyrite," Geol. Geofiz. **39** (7), 924–933 (1998).
20. V. L. Tauson, "Gold Solubility in the Common Gold-Bearing Minerals: Experimental Evaluation and Application to Pyrite," Eur. J. Mineral. **11**, 937–947 (1999).
21. J. R. Mycroft, G. M. Bancroft, McIntyre, and J. W. Lorimer, "Spontaneous Deposition of Gold on Pyrite from Solutions Containing Au (III) and Au (I) Chlorides: I. A Surface Study," Geochim. Cosmochim. Acta **59**, 3351–3365 (1995).
22. M. J. Scaini, G. M. Bancroft, and S. W. Knipe, "Au XPS, AES, and SEM Study of the Interactions of Gold and Silver Chloride Species with PbS and FeS_2: Comparison to Natural Samples," Geochim. Cosmochim. Acta **61**, 1223–1231 (1997).
23. A. A. Shtertser, "Pressure Transfer in Porous Materials during Explosions," Fiz. Goreniya Vzryva, No. 5, 113–119 (1988).
24. V. F. Nesterenko, "Shock Wave Methods for Producing and Compacting Rapidly Chilled Materials," Fiz. Goreniya Vzryva, No. 6, 85–98 (1985).
25. A. A. Marakushev, O. S. Bogatyrev, A. D. Fenogenov, *et al.*, "Impactogenesis and Volcanism," Petrologiya **1** (6), 571–596 (1993).
26. I. K. Karpov, V. S. Zubkov, V. A. Bychinskii, *et al.*, "Detonation in Mantle Flows of Heavy Hydrocarbons," Geol. Geofiz., No. 6, 754–763 (1998).
27. V. V. Adushkin and Yu. I. Zetser, "Energy Redistribution in Inner and Outer Geospheres during High Energy Impacts (Geophysics of Strong Disturbances)," in *Dynamic Processes in Geospheres: Geophysics of Strong Disturbances*, Ed. by Yu. I. Zetser (Nauka, Moscow, 1998), pp. 10–18 [in Russian].
28. L. W. Alvarez, W. Alvarez, F. Asaro, and H. V. Michel, "Extraterrestrial Cause for the Cretaceous–Tertiary Extinction," Science **208**, 1095–1108 (1980).
29. E. M. Galimov, A. G. Mironov, and S. M. Zhmodik, "Origin of Carbon in Strongly Carbonized Rocks of the Eastern Sayan," Geokhimiya, No. 1, 73–77 (2000). [Geochem. Int., **38**, 317–322 (2000)].
30. F. A. Letnikov, "Diamond Formation in Deep Tectonic Zones," Dokl. Akad. Nauk SSSR **271** (2), 433–435 (1983).
31. A. S. Alekseev, D. D. Badyukov, and M. A. Nazarov, "Cretaceous–Paleogene Boundary and Related Events," in *Impact Craters at the Cretaceous–Paleogene Boundary* (Nauka, Leningrad, 1990), pp. 8–24 [in Russian].
32. V. L. Masaitis, "Mass Concentration Trend in Impact Glasses and Tectites," in *Cosmochemistry and Comparative Planetology* (Nauka, Moscow, 1989), pp. 142–149 [in Russian].
33. V. I. Fel'dman, *Petrology of Impactites* (Mosk. Gos. Univ., Moscow, 1990) [in Russian].
34. M. A. Nazarov, Doctoral Dissertation in Geology and Mineralogy (GEOKhI, Moscow, 1995).
35. G. Schmidt, "Clues to the Nature of the Impacting Bodies Front Platinum Group Elements (Rhenium and Gold) in the Borehole Samples from the Clearwater East Crater (Canada) and the Boltgsh Impact Crater (Ukraine)," Meteorit. Planet. Sci. **32**, 761–767 (1997).